

Ultrathin perpendicular free layers for lowering the switching current in STT-MRAM

Tiffany S. Santos,^{1, a)} Goran Mihajlović, Neil Smith, J.-L. Li, Matthew Carey, Jordan A. Katine, and Bruce D. Terris

Western Digital Research Center, Western Digital Corporation, San Jose, CA 95119

(Dated: 5 August 2020)

The critical current density J_{c0} required for switching the magnetization of the free layer (FL) in a spin-transfer torque magnetic random access memory (STT-MRAM) cell is proportional to the product of the damping parameter, saturation magnetization and thickness of the free layer, $\alpha M_S t_F$. Conventional FLs have the structure CoFeB/nonmagnetic spacer/CoFeB. By reducing the spacer thickness, W in our case, and also splitting the single W layer into two layers of sub-monolayer thickness, we have reduced t_F while minimizing α and maximizing M_S , ultimately leading to lower J_{c0} while maintaining high thermal stability. Bottom-pinned MRAM cells with device diameter in the range of 55–130 nm were fabricated, and J_{c0} is lowest for the thinnest (1.2 nm) FLs, down to 4 MA/cm² for 65 nm devices, $\sim 30\%$ lower than 1.7 nm FLs. The thermal stability factor Δ_{dw} , as high as 150 for the smallest device size, was determined using a domain wall reversal model from field switching probability measurements. With high Δ_{dw} and lowest J_{c0} , the thinnest FLs have the highest spin-transfer torque efficiency.

I. INTRODUCTION

A leading challenge for the realization of a high-density STT-MRAM product is to have a low critical current required for switching the magnetization of the free layer, while maintaining high thermal stability for data retention. One route to reducing J_{c0} is to lower $M_S t_F$.¹ However, reducing M_S is known to increase the temperature dependence of the magnetic anisotropy and thermal stability factor,² which leads to poor retention at elevated operating temperature. Rather than reducing M_S , the approach taken in this study is to reduce t_F while maximizing M_S . Conventional free layers have the structure CoFeB/nonmagnetic spacer/CoFeB with a total thickness close to 2 nm. The role of the nonmagnetic spacer—typically metals such as Ta, W or Mo—is to absorb the boron atoms during the anneal step needed for solid-phase epitaxy of the MgO barrier and the CoFeB electrodes, which is critical for achieving high tunnel magnetoresistance (TMR)^{3,4} and high interfacial perpendicular anisotropy.^{5–7} The drawbacks for inserting these boron-sink materials are that they increase the damping constant of the FL, which is disadvantageous for lowering J_{c0} , and they create regions of low or zero moment in the free layer, referred to as a dead layer, which reduce volume-averaged M_S .

In this study the strategy for increasing M_S was to reduce the spacer thickness (and thus the dead layer) as much as possible, while still maintaining perpendicular anisotropy. Thicker CoFeB films need thicker spacer layers to stabilize perpendicular anisotropy. Hence, continuous reduction in spacer thickness necessitated a reduction in FL thickness. We found that thinner FLs with thinner spacer layers have higher M_S . Our film characterization

shows that FL properties improved by reducing t_F down to 1.2 nm and splitting the single spacer layer into two thinner spacer layers. Our ultrathin FLs have M_S reaching above 1700 emu/cm³ with no dead layer and with α of only 0.003. We tested devices with t_F in the range of 1.2–1.7 nm and device size down to ~ 55 nm. Our device testing shows that J_{c0} is lower for the thinner FLs while the thermal stability factor for domain wall reversal Δ_{dw} remains high, so that overall there is an increase in spin-transfer torque efficiency, defined as Δ_{dw}/I_{c0} where I_{c0} is the critical switching current.

II. EXPERIMENTAL METHOD

The STT-MRAM stacks in this study consist of the following layer structure: bottom electrode/seed layer/CoFeB reference layer/MgO tunnel barrier/free layer/MgO cap/Ru/Ta/Ru top electrode. In these bottom-pinned stacks, a Co/Pt-based synthetic antiferromagnet (SAF) was used to pin the magnetization of the reference layer. These stacks were sputtered at room temperature using an Anelva-7100 system and then postannealed at 335°C for 1 hour. The MgO layers were RF-sputtered from a MgO target.

In order to study the magnetic properties of the FL without any additional magnetic signal from the SAF or reference layer in the full STT-MRAM stack, the following FL-only stacks were prepared on oxidized Si substrates (thickness in nm): bottom electrode/3 Ta/5 Ru/0.3 W/0.5 CoFeB/1 MgO/FL/0.7 MgO/Ru. The 0.5 nm CoFeB seed layer is nonmagnetic at room temperature. The magnetic properties of the FL in the FL-only stack closely match those of the identical FL deposited in the bottom-pinned MRAM stack.

A FL thickness ladder of the following thicknesses were prepared: 1.2, 1.3, and 1.7 nm. For each thickness, two FL designs were compared: one with a single tungsten

^{a)}Electronic mail: tiffany.santos@wdc.com

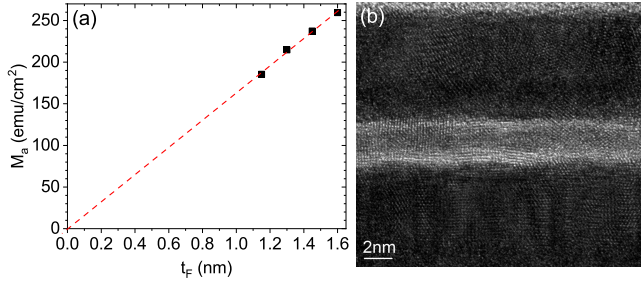


FIG. 1. a) Saturation moment divided by sample area M_a versus t_F for a FL-only thickness ladder with the structure CoFeB/CoFe/0.6 Mg/0.02 W/CoFe/0.6 Mg/0.02 W/CoFe, in which only the CoFeB and CoFe thicknesses are varied. The linear fit intersects the x-axis at 0 nm, indicating that there is no dead layer. b) Cross-section TEM of the $t_F=1.3$ nm sample with moment shown in (a) and structure given in Table I.

spacer (referred to as single-W) and the other with two tungsten spacers (referred to as split-W). For a given FL thickness, the combined W thickness of the two W layers in the split-W FL is equivalent to the thickness of the single W spacer in the single-W FL. The total W thickness is designated as t_W . The single-W FLs have the following layer structure, listed in order as sputtered on top of the MgO barrier: CoFeB/CoFe/Mg/W/CoFe. The split-W FLs have the following layer structure: CoFeB/CoFe/Mg/W/CoFe/Mg/W/CoFe. Refer to Table I for the nominal thickness of every layer for each FL in this study. The Mg layers are sacrificial layers that protect the previously sputtered CoFe film from damage caused by the impinging W atoms during deposition of the W spacer, as described in Ref. 8. In agreement with Ref. 8, we have found that no Mg remains in the FL.⁹ The Mg thickness used here was determined by optimizing for highest $M_S H_k$ of the free layer. M_S and anisotropy field H_k were determined from hard-axis magnetization versus magnetic field $M(H)$ loops of unpatterned films measured by vibrating sample magnetometry (VSM).

The t_F reported here is the nominal film thickness and includes the thickness of all the CoFeB, CoFe and W components. The nominal film thickness was determined using sputter time, and the sputter rate (i.e. nm/s) was calibrated for thick films using x-ray reflectivity. Thus, as the nominal W layer thickness is well below the thickness of a W atom, the W layer thickness refers to a partial monolayer of W atoms. As shown in the plot of saturation moment per area versus t_F in Fig. 1a for our split-W free layer design with $t_W=0.04$ nm, the linear fit line intersects the x-axis at 0 nm, indicating that there is no dead layer. A cross-section transmission electron micrograph (TEM) of the split-W FL-only film with $t_F=1.3$ nm is shown in Fig. 1b. The 1.0 nm thick MgO barrier and the 0.7 nm MgO cap are easily identified, with the 1.3 nm free layer in between the MgO layers.

Vector network analyzer ferromagnetic resonance (VNA-FMR) measurements were performed on the un-

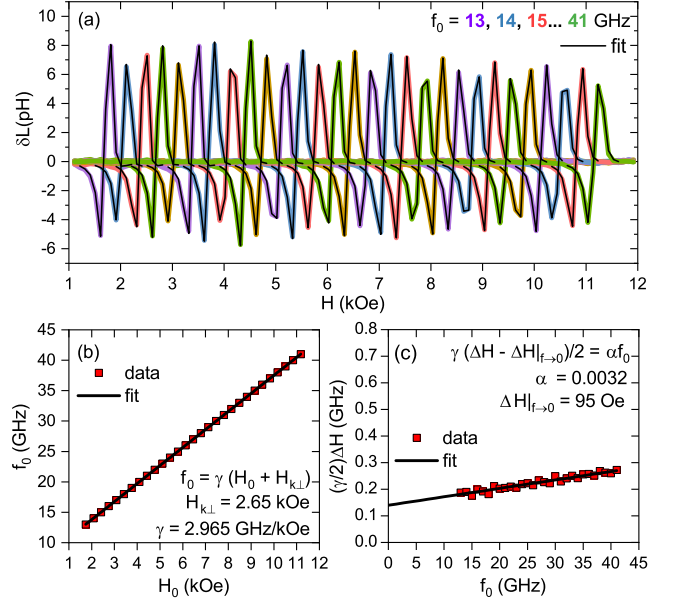


FIG. 2. FMR data for the split-W FL with $t_F=1.3$ nm. (a) From VNA-measured $S_{21}(H; f_0)$, extracted $\delta L(H; f_0) = -(50\Omega/\pi f_0)\delta \ln |S_{21}|$, the magnetic film contribution to lossy component of inductance of coplanar waveguide and sample, where “ δ ” implies a *finite* difference, e.g., $\delta L(H; f_0) = L(H + \delta H; f_0) - L(H - \delta H; f_0)$. Here, $\delta H=100$ Oe. The black lines are least squares fits: $\delta L(H; f_0) \propto \text{Im} \delta \chi(H) \cos \phi(f_0) - \text{Re} \delta \chi(H) \sin \phi(f_0)$, where $\chi(H) \propto (H - H_0 - i\Delta H/2)^{-1}$ with fit parameters $H_0(f_0)$, linewidth $\Delta H(f_0)$, and phase ϕ to account for other loss factors.¹⁰ (b) Linear fit: $f_0 = \gamma(H_0 + H_{k\perp})$ to obtain γ and $H_{k\perp}$. (c) Linear fit: $\gamma(\Delta H - \Delta H|_{f \rightarrow 0})/2 = \alpha f_0$ to obtain $\Delta H|_{f \rightarrow 0}$ and α .

patterned, FL-only films to determine the effective anisotropy field $H_{k\perp}$, the damping parameter α , and inhomogeneous linewidth broadening $\Delta H|_{f \rightarrow 0}$. The applied field H perpendicular to the film plane was swept once from 12 kOe to 1 kOe while transmission coefficients $S_{21}(H; f)$ were simultaneously measured at 29 discrete frequencies in the range $f_0=13$ –41 GHz. See Fig. 2 for an example. Inhomogeneous broadening originates from non-uniformities of the anisotropy, and thus it is an indicator of film uniformity. Lower $\Delta H|_{f \rightarrow 0}$ indicates better film uniformity.

Device performance was compared for the FLs in the thickness ladder, specifically the six free layers described in rows 2-4 of Table I. Bottom-pinned STT-MRAM test devices were fabricated using 193 nm deep UV optical lithography, followed by reactive ion etching of a hard mask, ion milling of the MRAM film, SiO₂ refill and then chemical mechanical planarization. Four different device sizes were fabricated for each FL, resulting in median electrical diameters D in the range of 55 to 130 nm. Device diameter was determined from the measured device resistance in the parallel state R_P and the resistance-area product RA , as $D = \sqrt{4RA/\pi R_P}$. The RA product, along with TMR ratio, was measured using the current-

TABLE I. Nominal thickness (in nm) of each layer within the FLs compared in this study. The single-W free layers have the structure: CoFeB/CoFe/Mg/W/CoFe, and the split-W free layers have the structure: CoFeB/CoFe/Mg/W/CoFe/Mg/W/CoFe.

t_F	t_W	single-W					split-W							
		CoFeB	CoFe	Mg	W	CoFe	CoFeB	CoFe	Mg	W	CoFe	Mg	W	CoFe
1.22	0.04	0.47	0.31	1.00	0.04	0.40	0.47	0.11	0.60	0.02	0.26	0.60	0.02	0.34
1.20	0.015	0.47	0.31	1.00	0.015	0.40	0.47	0.11	0.60	0.008	0.26	0.60	0.007	0.34
1.30	0.04	0.52	0.32	1.00	0.04	0.42	0.52	0.10	0.60	0.02	0.32	0.60	0.02	0.32
1.70	0.12	0.73	0.32	1.00	0.12	0.53	0.73	0.11	0.60	0.06	0.37	0.60	0.06	0.37

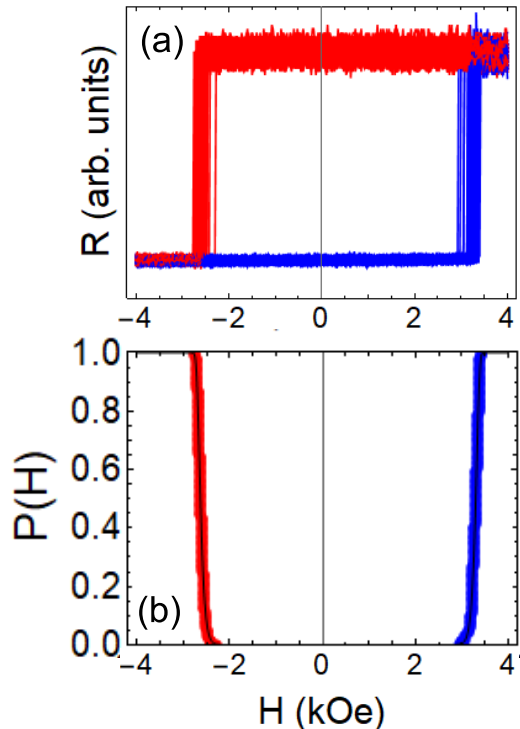


FIG. 3. (a) Resistance R versus field loops for a 63 nm device with a split-W FL having $t_F=1.3$ nm. (b) Empirical $P(H)$ corresponding to the switching fields in (a). The black line is the fit to a domain wall reversal model,¹² yielding $\varepsilon_{dw}=8.4$ erg/cm², $w_{dw}=12.5$ nm and $\Delta_{dw}=164.1$ for this device.

in-plane-tunneling (CIPT) technique¹¹ on identical, un-patterned film stacks sputtered within the same batch as the device wafers.

To determine Δ_{dw} for the FLs in the devices, we measured empirical field-switching probability distributions $P(H)$, whereby 100 resistance versus field transfer loops were measured at low bias (10mV, to eliminate spin-transfer torque effects) using a staircase ramp with a field step of 5 Oe and a dwell time of 0.2 ms. An example is shown in Fig. 3a for a device with diameter 63 nm and split-W FL with $t_F=1.3$ nm. Because the reversal mechanism for the FL magnetization in devices with diameters larger than 50 nm that we have studied here is by do-

main wall nucleation and propagation,^{13,14} $P(H)$ was fit using a domain wall reversal model.¹² An example of the fit is shown as black lines in Fig. 3b. The fit parameters are domain wall energy density ε_{dw} and domain wall width w_{dw} , and Δ_{dw} is given as $\Delta_{dw} = D\varepsilon_{dw}t_F/k_B T$, where k_B is the Boltzmann constant and T is temperature. Using the following relations between ε_{dw} and w_{dw} , we calculate exchange constant A_{ex} :

$$\varepsilon_{dw} = 4\sqrt{\frac{1}{2}M_S H_k A_{ex}} \quad (1)$$

$$w_{dw} = 2 \ln 2 \sqrt{\frac{2A_{ex}}{M_S H_k}} \quad (2)$$

$$A_{ex} = \frac{w_{dw}\varepsilon_{dw}}{8 \ln 2} \quad (3)$$

The J_{c0} was obtained by fitting the pulse width (t_P) dependence of switching voltage V_c , measured in the range of 5 μ s - 5 ms as described in Ref. 15, to the thermal activation model for spin-transfer torque switching.^{16,17} The switching voltage V_{c0} (defined at zero temperature and infinitely long time) is the intercept of the linear fit for V_c versus $\ln t_P$, and $J_{c0} = V_{c0}/RA$.

III. RESULTS AND DISCUSSION

A. Film properties

We first compare the magnetic properties for a single-W FL and a split-W FL with the same nominal $t_F = 1.22$ nm and $t_W = 0.04$ nm. Figures 4a and 4e display the easy axis and hard axis $M(H)$ loops, respectively, for the FLs described in the first row of Table I. The split-W FL has a slightly higher M_S and sharper switching (more square loop), as seen in the easy axis $M(H)$, and higher anisotropy field, as seen in the hard axis $M(H)$. The M_S and FMR results are listed in Table II. Splitting the W spacer from a single 0.04 nm layer to two 0.02 nm layers resulted in a sizeable increase of $H_{k\perp}$ from 3.02 kOe to 4.07 kOe and more than 3-fold reduction of $\Delta H|_{f\rightarrow 0}$, signifying a more uniform film. The low damping constant was maintained at $\alpha = 0.004$.

It has been our observation that $\Delta H|_{f\rightarrow 0}$ measured at the film level has a negative correlation to the coercive

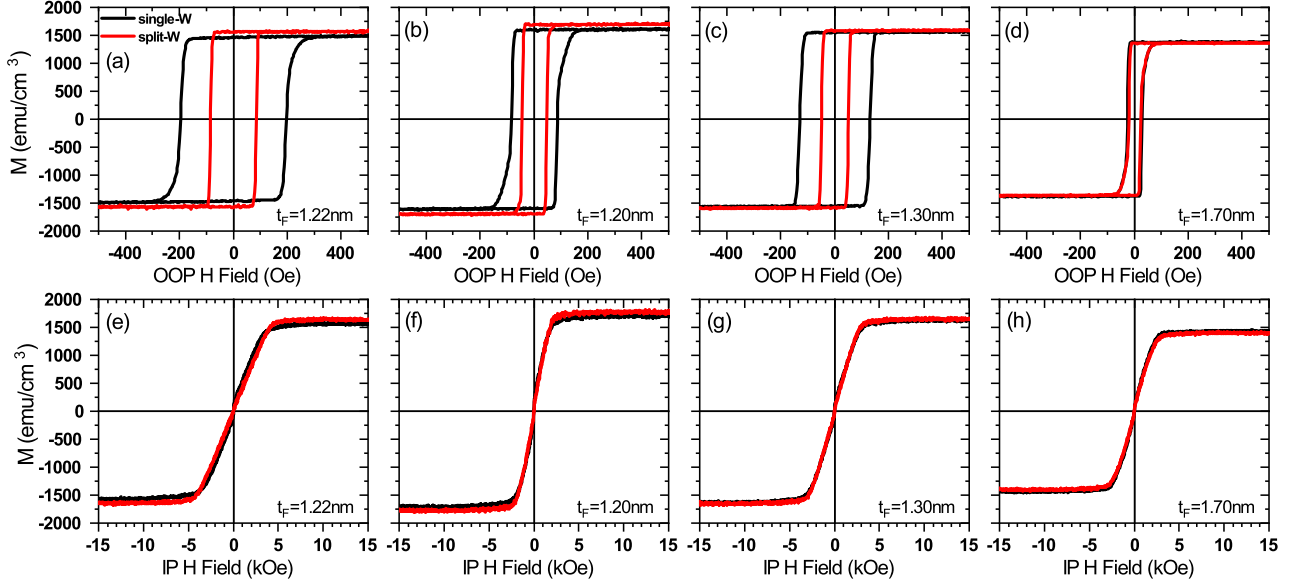


FIG. 4. $M(H)$ loops for FL-only films with the indicated t_F , for H applied out-of-plane (OOP) along the easy axis (a,b,c,d) and for H applied in-plane (IP) along the hard axis (e,f,g,h). Description of all samples is in Table I, and the M_S values are listed in Table II.

field H_C at the device level; higher $\Delta H|_{f \rightarrow 0}$ typically results in low H_C , regardless of H_k . Therefore, it is desirable to minimize $\Delta H|_{f \rightarrow 0}$ as much as possible. In order to lower $\Delta H|_{f \rightarrow 0}$ even further, we reduced the thickness of the W spacer. Figures 4b and 4f display the $M(H)$ loops for the single-W and split-W FLs for which t_W was reduced to 0.015 nm (refer to the second row in Table I). As is typical when reducing the W spacer thickness, we observed higher M_S , lower $H_{k\perp}$ and lower α , compared to the $t_W = 0.04$ nm FLs. Importantly, there was another significant reduction of $\Delta H|_{f \rightarrow 0}$ when going from single- to split-W spacers, dropping to <100 Oe which is promising for high H_C at the device level.

For the $t_F=1.3$ nm and 1.7 nm films in the FL thickness ladder of this study, the $M(H)$ loops are displayed in Figures 4c,g and 4d,h, respectively, and the magnetic properties are listed in Table II. Thicker FLs require more W in order to maintain perpendicular anisotropy, which results in lower M_S . Therefore, M_S is highest for the thinnest FLs. As demonstrated above, $H_{k\perp}$ can be tuned by the W amount. The W amount used here is the minimum amount necessary to maintain perpendicular anisotropy. $\Delta H|_{f \rightarrow 0}$ is significantly lower for the split-W FLs compared to the single-W FLs, with the exception of the 1.7 nm FLs, for which there appears to be no advantage to having two spacers as all parameters are nearly the same for the two designs. Notably, contrary to the common observation that α and $\Delta H|_{f \rightarrow 0}$ increase for thin CoFeB,^{18–20} α is very low for all of these ultrathin FLs, which is advantageous for achieving lower switching current.

B. Device Performance

The TMR for the six FLs is shown versus electrical diameter in Fig. 5a. This TMR measured for the devices closely matches the TMR values measured by CIPT (not shown). TMR is lower for the thinner FLs. In addition, TMR is lower for the split-W FLs. In general, lower TMR is observed for thinner free layers.^{21,22} More specifically in our FLs, in the single-W FL stack as t_F becomes thinner, the amount of CoFeB and CoFe between the MgO barrier and the W spacer becomes thinner, which means that the W atoms are closer to the MgO barrier. Any W atoms near the MgO/CoFeB interface are expected to disrupt the solid-phase epitaxy across this interface and thus disturb the coherent tunneling that otherwise generates high TMR.³ The W atoms are even closer to the MgO/CoFe interface in the case of the split-W FLs, which is thought to cause the TMR to be even lower.

The device coercivity H_C (see Fig. 5b) is in the range of ~ 2.2 – 2.6 kOe for the smallest device size for all FL designs, with the exception of the 1.2 nm single-W FL, which has the lowest film-level $H_{k\perp}$ and highest $\Delta H|_{f \rightarrow 0}$.

The results of the field switching probability test with data fit to a domain wall reversal model is displayed in Figure 6a-c. The w_{dw} for all FLs is the range of 12–17 nm. The 1.2 nm and 1.3 nm split-W FLs have the highest ε_{dw} . When multiplied by free layer volume to calculate Δ_{dw} , we find that all FLs, with the exception of the single-W 1.2 nm FL (having low H_C), have similarly high Δ_{dw} in the range of 130–150 for the smallest device size. Notably, for the split-W FLs, we have reduced t_F from 1.7 nm to 1.2 nm without significant loss of Δ_{dw} , while J_{c0} drops by a third with this t_F reduction,

TABLE II. Materials parameters for all FLs in this study: M_S values measured by VSM, FMR results ($H_{k\perp}$, α , and $\Delta H|_{f\rightarrow 0}$), and A_{ex} determined from devices using Equation 3. The parameter values are expressed to the last significant digit based on the corresponding error analysis, except for α where the absolute error is 0.0003.

t_F (nm)	t_W (nm)	No. of W layers	M_S (emu/cm ³)	$H_{k\perp}$ (kOe)	α	$\Delta H _{f\rightarrow 0}$ (Oe)	A_{ex} ($\mu\text{erg/cm}$)
1.22	0.04	1	1572	3.02	0.0040	420	
1.22	0.04	2	1644	4.07	0.0037	125	
1.20	0.015	1	1714	1.44	0.0036	210	1.7
1.20	0.015	2	1783	1.72	0.0031	80	2.01
1.30	0.04	1	1634	2.55	0.0037	180	1.77
1.30	0.04	2	1651	2.65	0.0032	95	1.85
1.70	0.12	1	1435	1.98	0.0044	95	1.49
1.70	0.12	2	1400	2.05	0.0044	85	1.47

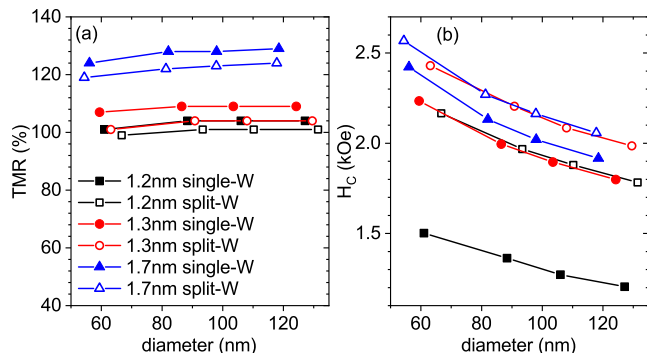


FIG. 5. Device TMR and coercivity H_C versus electrical diameter. Standard error of the mean is smaller than the data points.

as shown in Fig. 6d. Indeed, J_{c0} is lowest for the thinnest FLs with the split-W design, which have the lowest α (refer to Table II). Spin-transfer torque efficiency, defined as $\Delta_{\text{dw}}/I_{c0}$ and shown in Fig. 6e, is highest for the thinnest FLs with the split-W design.

The A_{ex} for each FL calculated using Equation 3 is listed in Table II. Overall, these A_{ex} values are high, approaching the values for bulk Fe (2.0 $\mu\text{erg/cm}$) and confirming the high quality of the FLs, in agreement with the film-level characterization. These values are similar to A_{ex} deduced from spin-wave spectroscopy for perpendicular CoFeB free layers in nanopillar magnetic tunnel junctions.^{23,24} For the 1.2 nm and 1.3 nm FL thicknesses, A_{ex} is higher for the split-W FL compared to the single-W FL, consistent with the superior properties observed at the film level for the split-W design (refer to Table II). Whereas for the two 1.7 nm FLs, the A_{ex} values are nearly the same, consistent with the other parameters for these films listed in Table II. When comparing A_{ex} across the thickness ladder for the split-W FLs, we observe higher A_{ex} for thinner W spacer, in agreement with the trend observed with the film-level magnetometry measurements of Ref. 25 and magneto-optical Kerr microscopy studies of Ref. 26.

As the film and device results for the 1.7 nm single-

W and split-W FLs are the same, one may conclude that there is no advantage to splitting the single W spacer into two spacers for this FL thickness, and that this split-W approach is only beneficial for thinner FLs. However, only one 1.7 nm split-W FL was explored in this study. By varying the thickness of the CoFeB and CoFe layers below, between, and above the two W spacers, it may be possible to tune M_S and H_k to achieve a 1.7 nm split-W FL design with superior performance. This would suggest some sensitivity to the proximity of the two W spacers to the MgO interfaces and to each other. Of course, thicker CoFeB between the MgO barrier and W spacer is desirable for higher TMR.

Lastly, we did attempt to extend our multi-spacer design beyond two W spacers, but any higher number of spacers resulted in a steep degradation of film properties. It becomes more challenging to control the thickness of even thinner W layers and to optimize more Mg sacrificial layers. The extreme end of the multi-spacer approach is a CoFeBW alloy free layer, though this is likely to result in lower M_S and lower Curie temperature.

IV. CONCLUSIONS

In summary, by minimizing the W spacer thickness in the FL, we have eliminated the dead layer, thereby maximizing M_S . We obtained optimal magnetic properties by splitting the W spacer layer into two thinner layers. For the FL thickness ladder in this study, from 1.2 nm to 1.7 nm, highest M_S was obtained for the thinnest FLs, while maintaining low damping constant and low inhomogeneous broadening of the FMR linewidth, signifying a more uniform and better quality film.

From device measurements, A_{ex} was highest for the thinnest FLs with split-W spacer, and thus high Δ_{dw} was maintained. We observed a thickness dependence of J_{c0} : the 1.2 nm FL has $\sim 30\%$ lower J_{c0} than the 1.7 nm FL. The thinnest FLs with split-W spacer have the lowest J_{c0} and highest spin-transfer-torque efficiency.

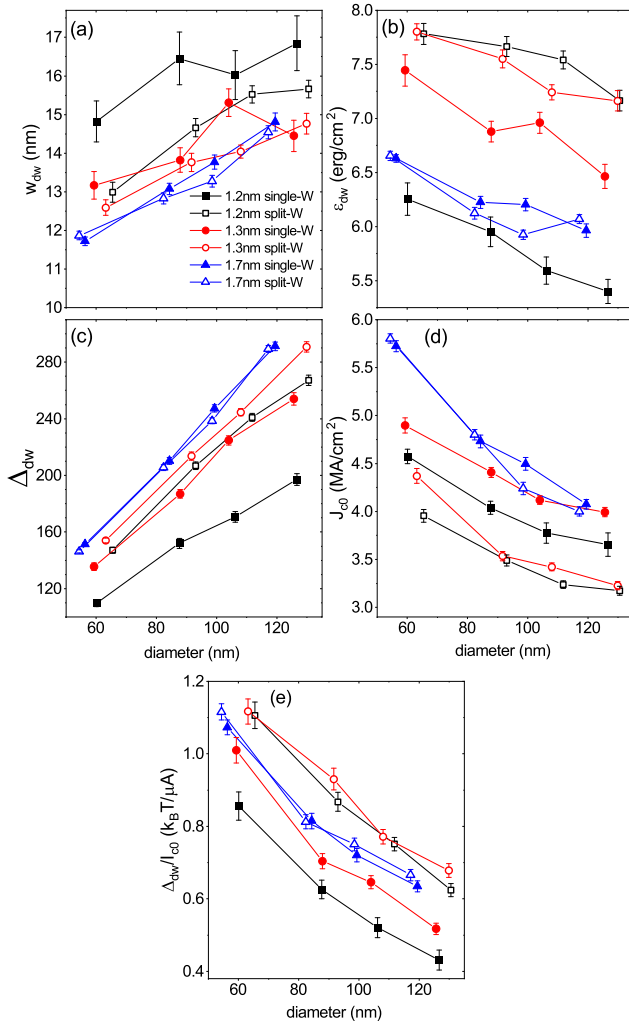


FIG. 6. (a) w_{dw} , (b) ε_{dw} , (c) Δ_{dw} , (d) J_{c0} and (e) Δ_{dw}/I_{c0} versus electrical diameter for all studied FLs. Each data point is the median value of approximately 35 measured devices, and the error bar is the standard error of the mean.

DATA AVAILABILITY

The data that supports the findings of this study are available within the article.

ACKNOWLEDGMENTS

The authors acknowledge Michael Gribelyuk, Loc Vinh and Xiaoyu Xu at the Western Digital Materials Laboratory for providing the high-resolution TEM analysis.

- ¹J. Z. Sun, Phys. Rev. B **62**, 570 (2000).
- ²J. M. Iwata-Harms, G. Jan, H. Liu, S. Serrano-Guisan, J. Zhu, L. Thomas, R.-Y. Tong, V. Sundar, and P.-K. Wang, Sci. Rep. **8**, 14409 (2018).
- ³W. H. Butler, X.-G. Zhang, T. C. Schulthess, and J. M. MacLaren, Phys. Rev. B **63**, 054416 (2001).
- ⁴J. Mathon and A. Umerski, Phys. Rev. B **63**, 220403(R) (2001).
- ⁵H. Sato, M. Yamanouchi, S. Ikeda, S. Fukami, F. Matsukura, and H. Ohno, Appl. Phys. Lett. **101**, 022414 (2012).
- ⁶J.-H. Kim, J.-B. Lee, G.-G. An, S.-M. Yang, W.-S. Chung, H.-S. Park, and J.-P. Hong, Sci. Rep. **5**, 16903 (2015).
- ⁷V. B. Naik, H. Meng, and R. Sbiaa, AIP Advances **2**, 042182 (2012).
- ⁸J. Swerts, S. Mertens, T. Lin, S. Couet, Y. Tomczak, K. Sankaran, G. Pourtois, W. Kim, J. Meerschaet, L. Souriau, D. Radisic, S. Van Elshocht, G. Kar, and A. Furnemont, Appl. Phys. Lett. **106**, 262407 (2015).
- ⁹As determined in a separate study of similar film stacks using cross-section transmission electron microscopy with elemental analysis using electron energy loss spectroscopy, in both the as-sputtered and post-annealed state.
- ¹⁰N. Smith, *unpublished*.
- ¹¹D. C. Worledge and P. L. Trouilloud, App. Phys. Lett. **83**, 84 (2003).
- ¹²G. Mihajlović, N. Smith, T. Santos, J. Li, B. D. Terris, and J. A. Katine, arXiv:2008.00412.
- ¹³L. Thomas, G. Jan, S. Le, Y.-J. Lee, H. Liu, S. Zhu, J. Serrano-Guisan, R.-Y. Tong, K. Pi, D. Shen, R. He, J. Haq, Z. Teng, A. Rao, V. Lam, Y.-J. Wang, T. Zhong, T. Torng, and P.-K. Wang, 2015 IEEE International Electron Devices Meeting (IEDM) , 26.4.1 (2015).
- ¹⁴G. D. Chaves-O'Flynn, G. Wolf, J. Z. Sun, and A. D. Kent, Phys. Rev. Appl. **4**, 024010 (2015).
- ¹⁵G. Mihajlović, N. Smith, T. Santos, J. Li, M. Tran, M. Carey, B. Terris, and J. Katine, Phys. Rev. Appl. **13**, 024004 (2020).
- ¹⁶R. H. Koch, J. A. Katine, and J. Z. Sun, Phys. Rev. Lett. **92**, 088302 (2004).
- ¹⁷Z. Li and S. Zhang, Phys. Rev. B **69**, 134416 (2004).
- ¹⁸X. Liu, W. Zhang, M. J. Carter, and G. Xiao, J. Appl. Phys. **110**, 033910 (2011).
- ¹⁹M. P. R. Sabino, S. T. Lim, and M. Tran, IEEE Trans. Magn. **50**, 6101404 (2014).
- ²⁰E. C. I. Enobio, H. Sato, S. Fukami, F. Matsukura, and H. Ohno, IEEE Mag. Lett. **6**, 5700303 (2015).
- ²¹H. Sato, M. Yamanouchi, K. Miura, S. Ikeda, R. Koizumi, F. Matsukura, and H. Ohno, IEEE Magn. Lett. **3**, 3000204 (2012).
- ²²L. Cuchet, B. Rodmacq, S. Auffret, R. Sousa, and B. Dieny, Appl. Phys. Lett. **105**, 052408 (2014).
- ²³A. Helmer, S. Cornelissen, T. Devolder, J.-V. Kim, W. van Roy, L. Lagae, and C. Chappert, Phys. Rev. B **81**, 094416 (2010).
- ²⁴T. Devolder, J.-V. Kim, L. Nistor, R. Sousa, B. Rodmacq, and B. Diény, J. Appl. Phys. **120**, 183902 (2016).
- ²⁵J. B. Mohammadi, B. Kardasz, G. Wolf, Y. Chen, M. Pinarbasi, and A. D. Kent, ACS Appl. Electron. Mater. **1**, 2025 (2019).
- ²⁶B. Buford, P. Dhagat, and A. Jander, IEEE Magn. Lett. **7**, 3107903 (2016).